Electronic Supplementary Material

Amorphous Conversion in Pyrolytic Symmetric Trinuclear Nickel Clusters Trigger Trifunctional Electrocatalysts

*Li Li[a], Hui-Feng Zhao[a], Mei-Xing Gan[b], Tao Zhang[a], Jia-Ning Li[b], Shi Tao[*c], Jing Peng[d], Hai-Bin Yu[*a] and Xu Peng[*b]*

[a]Wuhan National High Magnetic Field Center & School of Physic, Huazhong University of Science and Technology, Wuhan 430074, China
Email: haibinyu@hust.edu.cn (H. -B. Y.)
[b]College of Chemistry and Chemical Engineering, Hubei University, Wuhan 430062, China.
Email: pengxu@hubu.edu.cn (X. P.)
[c]School of Electronic and Information Engineering, Jiangsu Laboratory of Advanced Functional Materials, Changshu Institute of Technology, Changshu 215500, China.
Email: taoshi@cslg.edu.cn (S. T.)
[d]Shenzhen Key Laboratory of Energy Materials for Carbon Neutrality, Shenzhen Institutes of Advanced Technology, Chinese Academy of Sciences, Shenzhen 518055, China.

1. Experimental

Materials and Methods

Synthesis of Ligands (**H₃sal-dahp**) (2,2'-((1E,1'E)-((2-hydroxypropane-1,3-diyl)bis(azaneylylidene))bis(methaneylylidene))diphenol)

The preparation of the ligand H₃sal-dahp was followed as in a previous work[1], 1,3-diamino-2-hydroxypropane (4.51 g, 50 mmol) was dissolved in methanol (100 mL), stirred on a room temperature mixer for 10 min, and then the mixture of Salicylaldehyde (12.21 g, 100mmol) and methanol (200 mL) solution was slowly added, stirred and reacted at normal temperature for 5 h, vacuum filtered, washed with methanol and collected to obtain a large amount of pale yellow powder, dried at normal temperature for standby, 1,3-diamino-2-hydroxypropane salicylaldehyde ligand, Yield: 85% (based on salicylaldehyde).
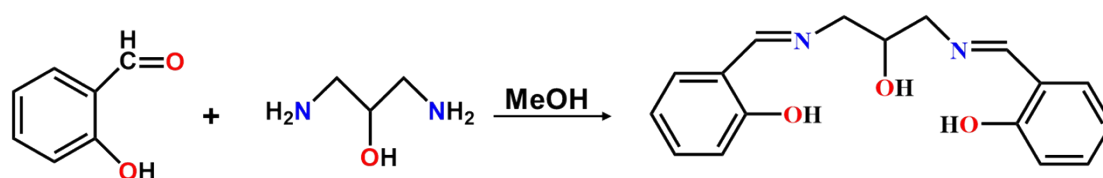

Figure S1. Schematic diagram and structure of H₃sal-dahp.

Synthesis of Ni₃(H₃sal-dahp)·2DMF

H₃sal-dahp(0.5 mmol, 0.149 g) and NiCl₂·6H₂O(0.5mmol, 0.120 g) in methanol/DMF (V/V=2:1) (15 mL) ,CH₃COOH (0.1 mL)were stirred for about 10 minutes and then 0.6 mL triethylamine was added. The mixture was placed in a 25 mL Teflon-lined autoclave and heated at 80 ºC for 24 h. The autoclave was cooled over a period of 8 h at a rate of 5ºC·h⁻¹, and yellow crystals were collected by filtration, washed with methanol, and dried in air. Yield: 30 % (based on Ni). Elemental analyses calcd for $C_{42}H_{50}N_6Ni_3O_{12}$: Ni,17.5; C, 50.09; H, 4.96; N, 8.35; O, 19.08 %. Found: Ni,17.3; C, 50.0; H, 4.50; N, 8.10 %.

Preparation of Ni₃-T (T represents pyrolysis temperature)

For these samples, the as-prepared precursor Ni₃(H₃sal-dahp)·2DMF was heated under a N₂ (80 mL·min⁻¹) atmosphere to the required temperature (200, 250, 285, 300, 325, 350, or 400 ºC) at a ramping rate of 5 ºC·min⁻¹ and kept at that temperature for 1 h followed by cooling to room temperature naturally. The samples are labeled Ni₃-200, Ni₃-250, Ni₃-285, Ni₃-300, Ni₃-325, Ni₃-350 and Ni₃-400, respectively.

Characterization

Thermogravimetric analyses (TGA) were performed under a flow of nitrogen at a heating

rate of 5 °C·min⁻¹ using a Netzsch TG 209 F3. Powder X-ray diffraction (PXRD) patterns were recorded on a Rigaku D/max-IIIA diffractometer (Cu Kα) at 293 K. Transmission electron microscopy (TEM) and High-resolution TEM (HR-TEM) images of the samples were obtained using a FEI Talos F200X transmission electron microscope (200 kV). X-ray photoelectron spectroscopy (XPS) was conducted on VG Microtech ESCA 2000 using a monochromic Al X-ray source, and the binding energies (BE) were calibrated by setting the measured binding energy of C 1s to 284.8 eV. Raman spectra were collected on a Renishaw System 1000 micro-Raman spectrometer. The thermogravimetric-mass analysis was performed on a Rigaku Thermo Mass Photo (TG-MS) with a Skimmer type mass spectrometer (MS/EI). The measurements were conducted in the range 30-900 °C at 5 °C·min⁻¹. Ni K-edge X-ray absorption fine structure spectroscopy (XAFS) was collected at the 1W1B beamline of Beijing Synchrotron Radiation Facillity (BSRF).

X-ray Crystallography

Single-crystal X-ray diffraction data for Ni_3 were collected on a Rigaku R-AXIS SPIDER IP diffractometer employing graphite-monochromated (Cu, λ = 1.54184 Å) using the θ-ω scan technique at 293 K. The structure was solved by direct methods using ShelXS and refined using full-matrix least-squares technique within the *SHELXL2015* and *OLEX.2* program packages. All non-hydrogen atoms were refined with anisotropic thermal factors. Crystallographic data for the structural analyses have been deposited at the Cambridge Crystallographic Data Center and given CCDC reference number 2270095. The supplementary crystallographic data for this compound can be found in the Table S1a, and selected bond lengths and angles are given in Table S1b.

X-ray total scattering and pair distribution function (PDF) analysis

X-ray total scattering data were collected at room temperature using Rigaku SmartLab X-ray diffractometer with Ag-source (λ=0.56 Å). Data collection was carried out using loaded 0.7 mm diameter quartz capillaries and collections conditions were:3-157 ° in 2θ, 0.05 ° step size, 0.5 °·min-1. Corrections for background, multiple scattering, container scattering, and absorption were applied using the SmartLab studioII.

Electrochemical Measurements

For Ni_3-based electrochemical tests in this paper were conducted under three electrode

room temperature conditions, using CHI760E from Shanghai Chenhua Company as the electrochemical workstation. The OER/UOR/MOR electrocatalytic performance of the catalysts was evaluated. All potential was transformed into reversible hydrogen electrodes through the following formula: E(RHE) = E(vs. $_{Hg/Hg2Cl2}$) + 0.241 + pH×0.059 V. Before evaluating the activity, the catalyst needs to activate for 100 cycles of CV with the voltage window of 1.0-1.5 V (vs. RHE) under the sweep speed of 50 mV s^{-1}. Linear sweep Voltammetry (LSV) was used to evaluate the activity of the catalyst for OER from 1.2-1.8 V vs. RHE at a scanning rate of 5 mV · s^{-1} (90% iR compensation) η= E_{RHE}-1.23 V yields the overpotential at a current density of 10mA · cm^{-2}. The Tafel slope is obtained by fitting the LSV curve, and the Tafel slope is: η = B log j+a, where b represents the fitted Tafel slope and j is the current density. Electrochemical impedance spectroscopy (EIS) is measured at a certain potential from 0.1-10000 Hz by applying an amplitude of 10 mV on the frequency window. The electrochemical double layer capacitance (C_{dl}) is measured by Cyclic voltammetry in the illegal pull interval, and the rates are 20, 40, 60, 80, 100 and 120 mV s^{-1} respectively. The epicyclic frequency is calculated according to the formula, where I is the current in amperes, F is the Faraday constant, and m is the number of moles of active catalyst (assuming that UOR activity involves all-metal sites). Cyclic voltammetry (CV) scanning at different scanning rates between narrow potentials (ν) Conduct the test and record half of the difference in anode current density (ja and jc) as Δ j,

i.e. $\Delta j = \dfrac{ja - jc}{2}$ (Eq. 1)

The electrochemical active surface area (ECSA) is calculated based on the C_{dl} value (Eq. 2), and the roughness factor (R_f) is also an important factor in determining electrochemical activity. The formula is as follows (Eq. 3):

$$ECSA = \dfrac{C_{dl}}{40\mu F\ cm^{-2} per cm^2 ECSA}$$ (Eq. 2)

$$RF = \dfrac{ECSA}{Geometric\ area\ of\ the\ eletrode}$$ (Eq. 3)

$$TOF = \dfrac{j * A}{n * F * N}$$ (Eq. 4)

In Eq. 4, j is the current density obtained under a given overvoltage, A is the surface area of the electrode (the total positive and negative area is about 0.25 cm^2), n is the number of electrons transferred in the electrocatalytic reaction, F is the Faraday constant (96485 C/mol),

and N is the number of moles of metal atoms on the electrode. Since some metal sites in the catalyst are electrochemically unpredictable, assuming that all metal ions exist on the reaction surface, calculate the epicyclic frequency (TOF) to evaluate the inherent activity of UOR catalyst.

We made the working electrode from carbon paper, cutting it to 0.5 cm × 3 cm beforehand. To prepare the working electrode, we dispersed 3 mg of catalyst into a solution containing 0.25 mL of isopropanol, 0.25 mL of ethanol, and 2 μL of 5 wt% Nafion, then ultrasonicated the suspension for 30 minutes. We then pipetted 4 μL of the suspension and dropwise applied it onto the treated carbon paper, with a dropwise area of 0.5×0.5 cm^2. The catalyst loading during OER testing was 1.44 mg · cm^{-2}. We conducted the urea oxidation experiment in a 1.0 M KOH + 0.33 M urea electrolyte, using the same testing method as for UOR, with a loading of 1.2 mg · cm^{-2}. The loading capacity of the MOR test sample was 0.96 mg · cm^{-2}.

DFT

The first-principles calculations were performed in the framework of density functional theory(DFT) using the Vienna ab-initio simulation package (VASP). The generalized gradient approximation (GGA) as formulated by Perdew-Burke-Ernzerhof (PBE) functional is adopted for the exchange-correlation potential. A cutoff energy of 400 eV is employed for the plane wave expansion of the wave finctions. The (11 x 1lx 8) gamma-centered k mesh is used for the Brillouin zone sampling. The van der Waals (vdW) interaction was included by using the DFT-D3method. For a285 crystal. All atoms were fully relaxed until the forces on unconstrained atoms were less than 0.0l eV Å-1, For density of states (DOS) and d-band center calculations, The DOS projected onto the d-states that interact with the adsorbate state can be characterized by the center of d-projected DOS:

$$\varepsilon d = \frac{\int_{-\infty}^{\infty} nd(\varepsilon)\varepsilon d\varepsilon}{\int_{-\infty}^{\infty} nd(\varepsilon)d\varepsilon}$$

2. Figures and Tables

Table S1. Crystallographic data for Ni₃(H₃sal-dahp)·2DMF.

Compounds	2(C₂₁H₂₄N₃Ni₁.₅O₆)
Formula	$C_{42}H_{50}N_6Ni_3O_{12}$
Formula weight	1007.01
T (K)	293
Crystal system	triclinic
Space group	*P-1*
a (Å)	10.6889(7)
b (Å)	14.1596(9)
c (Å)	15.3942(9)
α (°)	82.996(5)
β (°)	87.336(5)
γ (°)	68.730(6)
V (Å³)	2155.0(2)
Z	2
D_c.(g cm⁻³)	1.552
μ (mm⁻¹)	2.114
Reflns coll.	18905
Unique reflns	7664
R_{int}	0.0526
$R_1{}^a$[I ≥ 2σ(I)]	0.0683
$wR_2{}^b$ (all data)	0.2012
GOF	1.076

$^aR_1=\sum||F_o| - |F_c||/\sum|F_o|.$ $^bwR_2=[\sum w(F_o{}^2 - F_c{}^2)^2/\sum w(F_o{}^2)^2]^{1/2}.$

Table S2. Selected Bond lengths (Å) and angles (°) for **2(C$_{21}$H$_{24}$N$_3$Ni$_{1.5}$O$_6$)**.

Ni4-O10^1	2.085(3)	Ni4-O10	2.085(3)	Ni4-O7^1	2.103(3)
Ni4-O7	2.103(3)	Ni4 O8^1	2.132(3)	Ni4 O8	2.132(3)
Ni3 O9	2.054(3)	Ni3 O7	2.008(3)	Ni3 O8	2.027(3)
Ni3 O11	2.229(3)	Ni3 N4	2.025(3)	Ni3 N5	2.014(4)
Ni1 N1	2.012(4)	Ni1 N2	2.026(4)	Ni1 O5	2.215(3)
Ni1 O1	1.997(3)	Ni1 O2	2.029(3)	Ni1 O4	2.067(3)
Ni2 O1^2	2.090(3)	Ni2 O1	2.090(3)	Ni2 O2	2.096(3)
Ni2 O2^2	2.096(3)	Ni2 O3	2.100(3)	Ni2 O3^2	2.100(3)
O10^1-Ni4-O10	180.0	O10 Ni4 O7^1	92.84(12)	O10^1-Ni4-O7^1	87.16(12)
O10-Ni4-O7	87.16(12)	O10^1-Ni4-O7	92.84(12)	O10-Ni4-O8^1	90.47(12)
O10^1-Ni4-O8^1	89.53(12)	O10^1-Ni4-O8	90.47(12)	O10-Ni4-O8	89.53(12)
O7-Ni4-O7^1	180.0	O7-Ni4-O8^1	101.38(11)	O7^1-Ni4-O8^1	78.62(11)
O7^1-Ni4-O8	101.38(11)	O7-Ni4-O8	78.62(11)	O8^1-Ni4-O8	180.0
O9 Ni3 O11	175.03(12)	O7-Ni3-O9	92.71(12)	O7-Ni3-O8	83.37(11)
O7-Ni3-O11	90.41(12)	O7-Ni3-N4	171.02(15)	O7-Ni3-N5	90.39(13)
O8-Ni3-O9	94.02(13)	O8-Ni3-O11	90.17(12)	N4-Ni3-O9	92.94(14)
N4-Ni3-O8	89.28(14)	N4 Ni3 O11	84.44(14)	N5 Ni3 O9	89.68(15)
N5 Ni3 O8	172.87(13)	N5 Ni3 O11	86.44(14)	N5 Ni3 N4	96.61(15)

|					
C39 O10 Ni4	129.4(3)	C39 O9 Ni3	123.0(3)	Ni3-O7-Ni4	96.55(12)
C22-O7-Ni4	136.0(2)	C22-O7-Ni3	124.3(2)	Ni3-O8-Ni4	95.08(11)
C29-O8-Ni4	135.6(3)	C29-O8-Ni3	123.5(3)	C42-O11-Ni3	117.3(3)
C36-N4-Ni3	120.2(3)	C35-N4-Ni3	121.4(3)	C28-N5-Ni3	123.1(3)
C38 N5 Ni3	119.8(3)	C7 N1 Ni1	122.4(3)	C17-N1-Ni1	118.9(4)
C15 N2 Ni1	121.4(4)	C14 N2 Ni1	121.2(4)	C21-O5-Ni1	118.3(3)
C8 O1 Ni1	126.0(3)	C8 O1 Ni2	134.8(3)	Ni1-O1-Ni2	96.49(12)
C1 O2 Ni1	121.4(3)	C1 O2 Ni2	135.0(3)	Ni1-O2-Ni2	95.31(12)
C18-O4-Ni1	123.6(3)	C18-O3-Ni2	129.6(3)	N1-Ni1-N2	96.56(18)
N1 Ni1 O5	84.49(14)	N1 Ni1 O2	88.63(15)	N1 Ni1 O4	91.64(15)
N2 Ni1 O5	83.83(13)	N2 Ni1 O2	171.49(15)	N2 Ni1 O4	93.32(15)
O1 Ni1 N1	170.80(16)	O1 Ni1 N2	91.27(15)	O1 Ni1 O5	91.58(12)
O1 Ni1 O2	83.04(12)	O1 Ni1 O4	92.73(13)	O2 Ni1 O5	89.98(12)
O2 Ni1 O4	93.27(13)	O4 Ni1 O5	174.88(12)	O1^2 Ni2 O1	180.0
O1 Ni2 O2^2	100.78(11)	O1^2 Ni2 O2	100.78(11)	O1 Ni2 O2	79.22(11)
O1^2 Ni2 O2^2	79.22(11)	O1^2 Ni2 O3^2	89.39(12)	O1 Ni2 O3	89.38(12)
O1^2 Ni2 O3	90.62(12)	O1 Ni2 O3^2	90.61(12)	O2^2 Ni2 O2	180.0
O2 Ni2 O3^2	92.62(12)	O2 Ni2 O3	87.38(12)	O2^2 Ni2 O3	92.62(12)
O3^2 Ni2 O3	180.0				
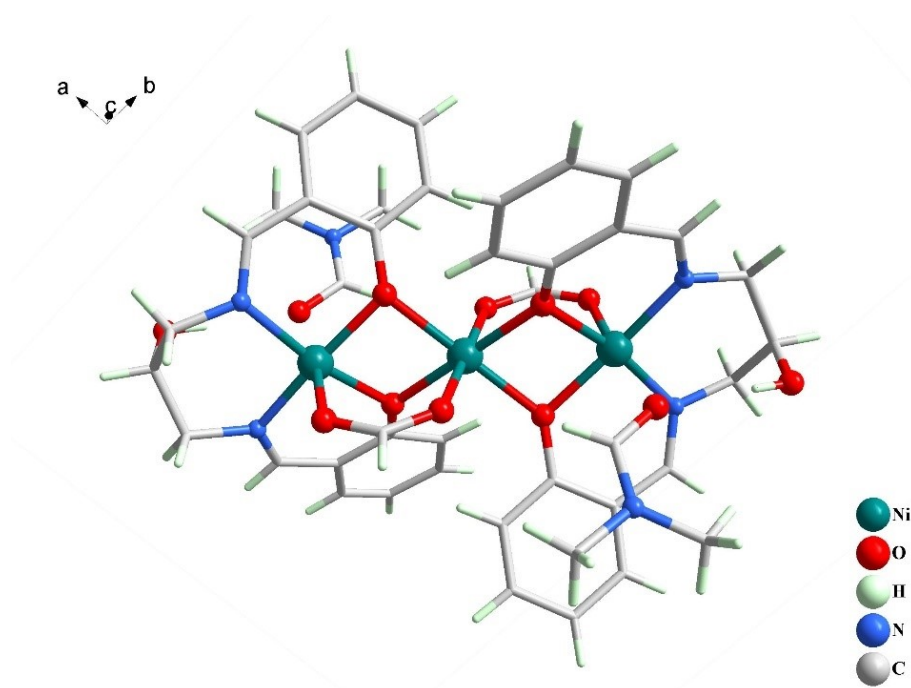
Figure S2. Structure of the component cationic cluster and the anion of $2(C_{21}H_{24}N_3Ni_{1.5}O_6)$.
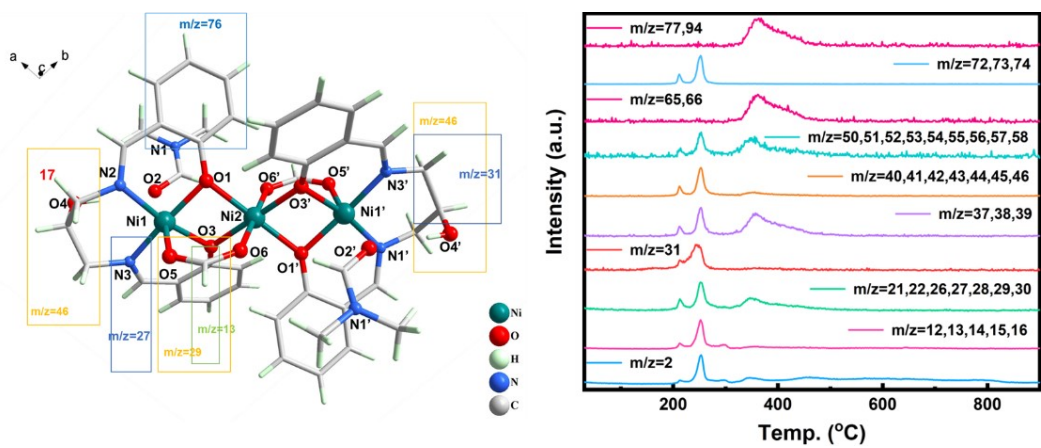
Figure S3. Possible generation of molecular fragments detected by TG-MS in the temperature range of 30 to 900 °C.
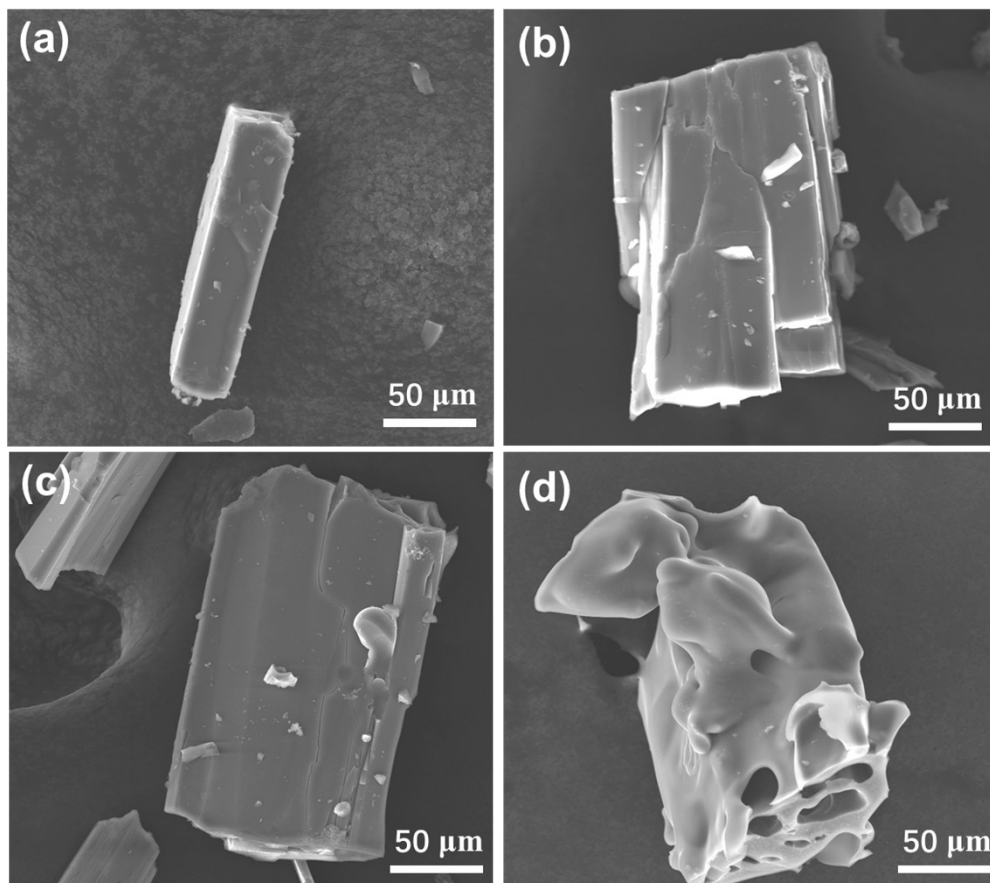
Figure S4. Scanning electron microscopy images of (a) a250. (b) a300. (c) c350. (d) c400.
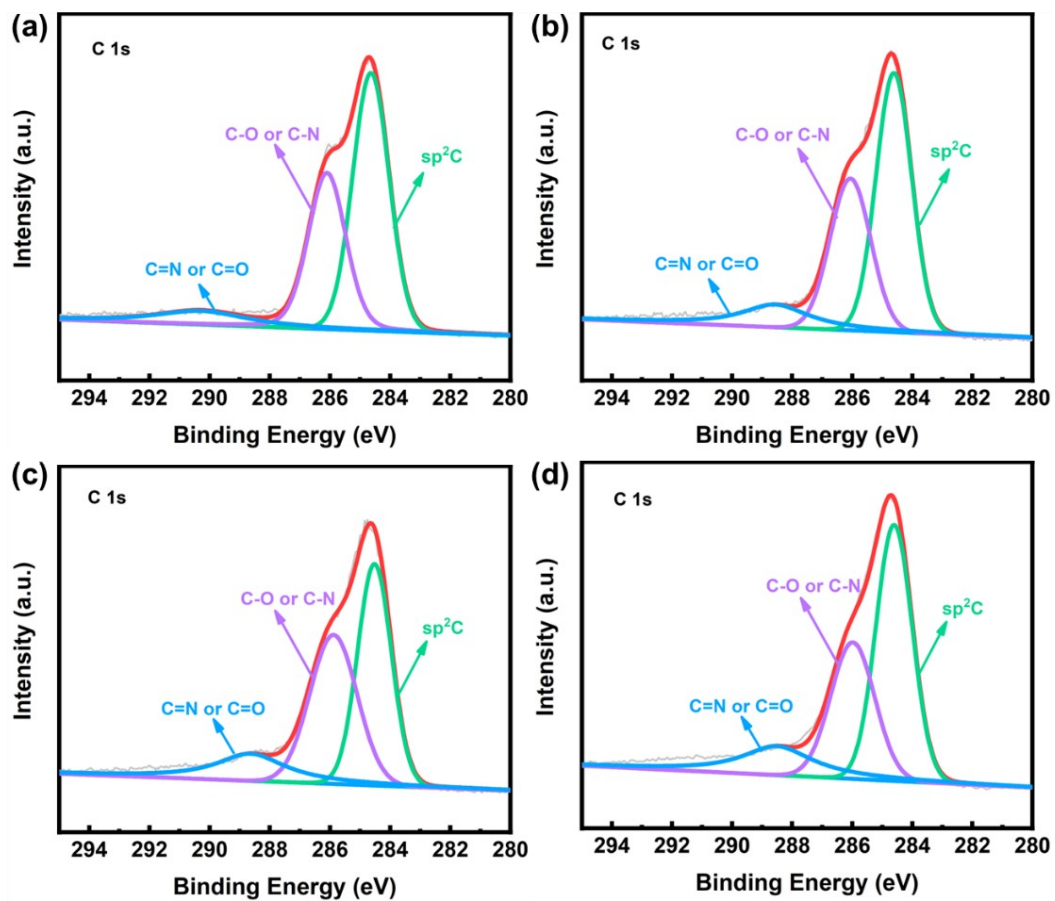
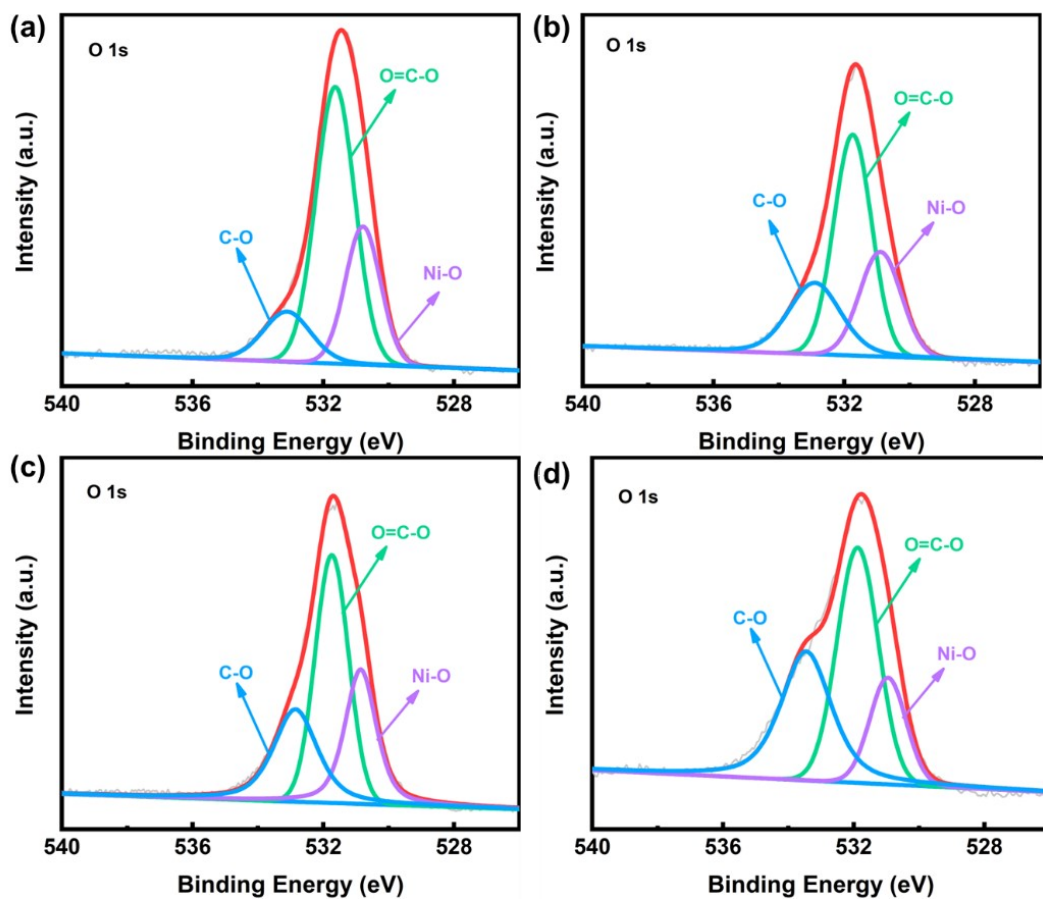**Figure S5**. High resolution XPS spectra of C 1s peak of (a) a250, (b) a285, (c) a300 and (d) c325.

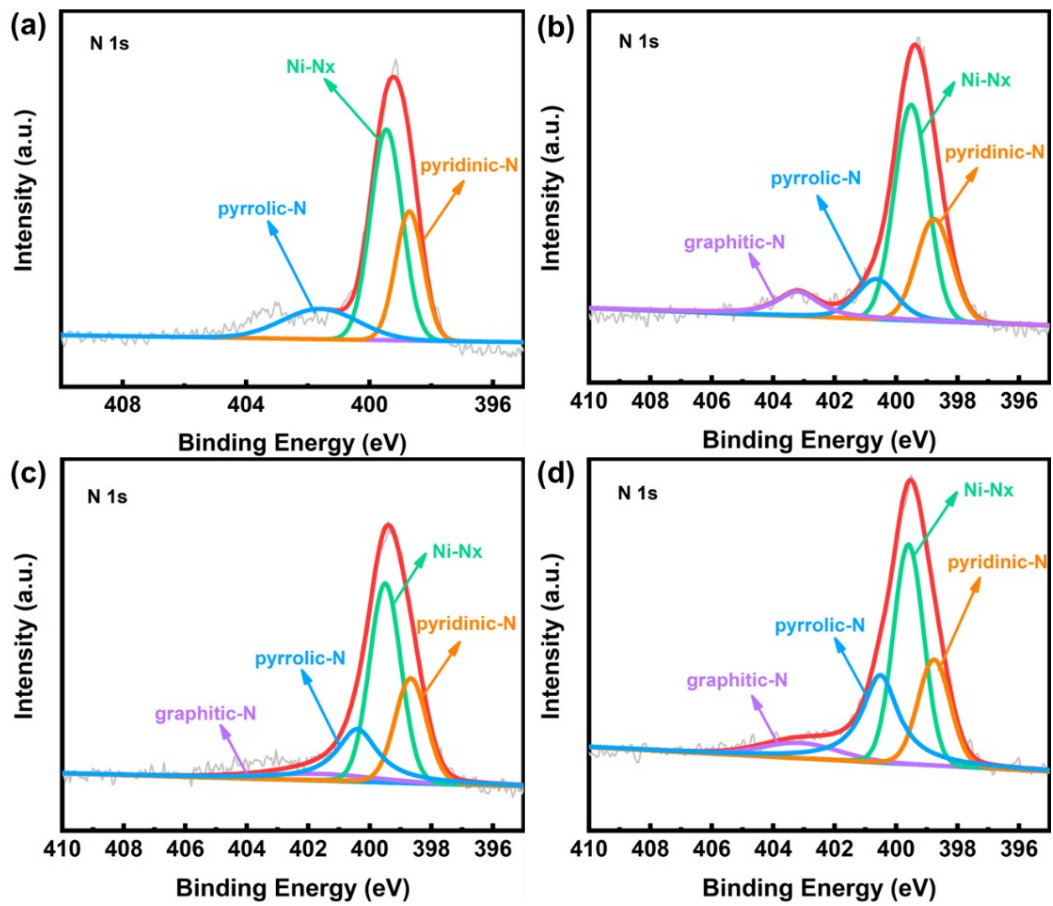**Figure S6**. High resolution XPS spectra of O 1s peak of (a) a250, (b) a285, (c) a300 and (d) c325.

Figure S7. High resolution XPS spectra of N 1s peak of (a) a250, (b) a285, (c) a300 and (d) c325.
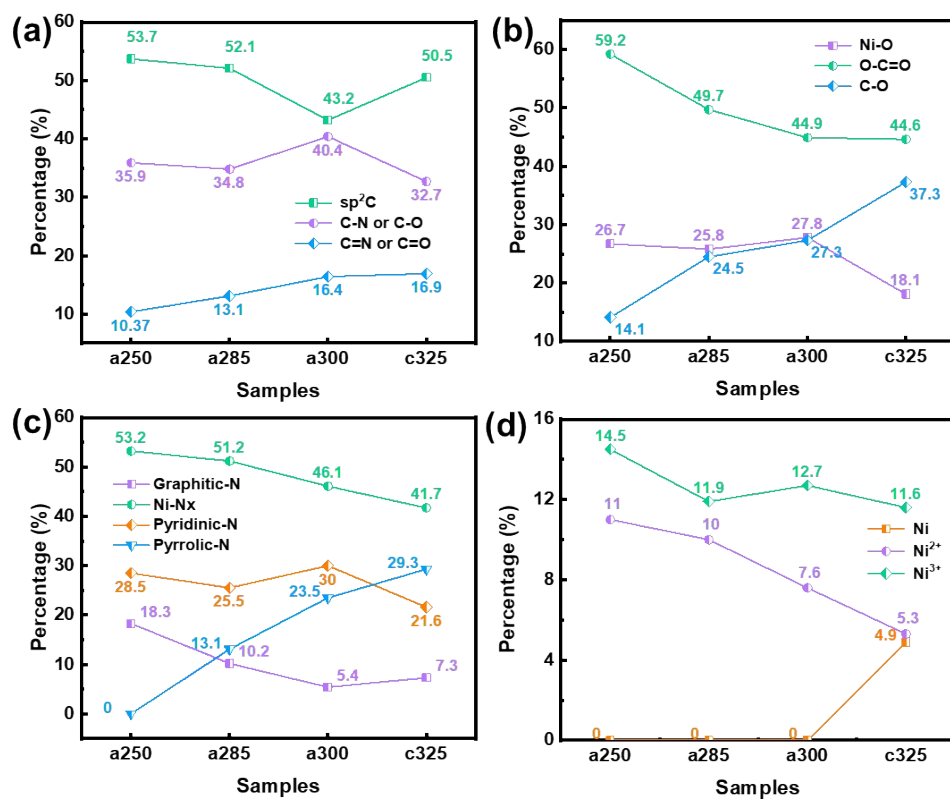
Figure S8. Change trend of content of different C species in C1s spectrum (b) O species in O1s spectrum (c) N species in N1s spectrum (d) Ni species in Ni2p spectrum.
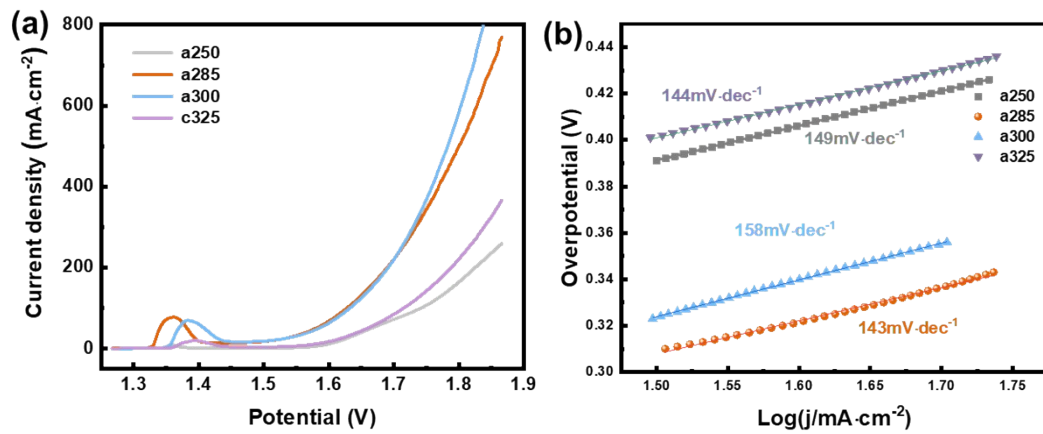
Figure S9. (a) LSV curves (b) Tafel plots of a250, a285, a300, c325 samples.
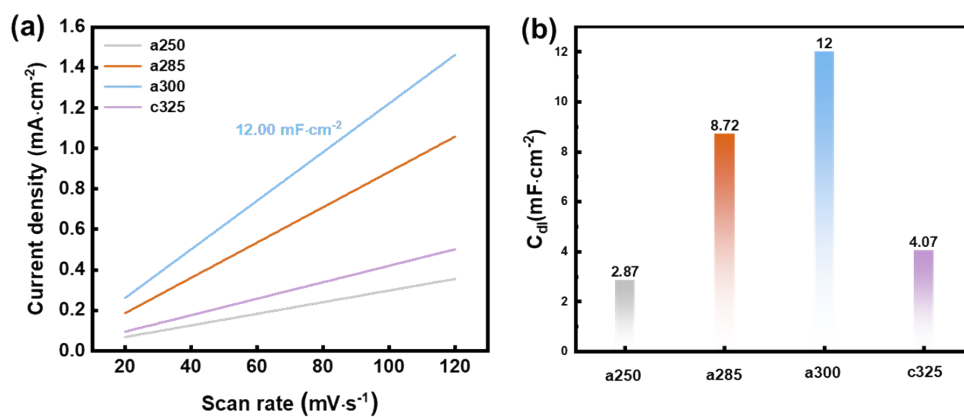
Figure S10. linear plots of cathodic charging current versus scan rate derived from CV diagrams for a250, a285, a300, c325 samples.
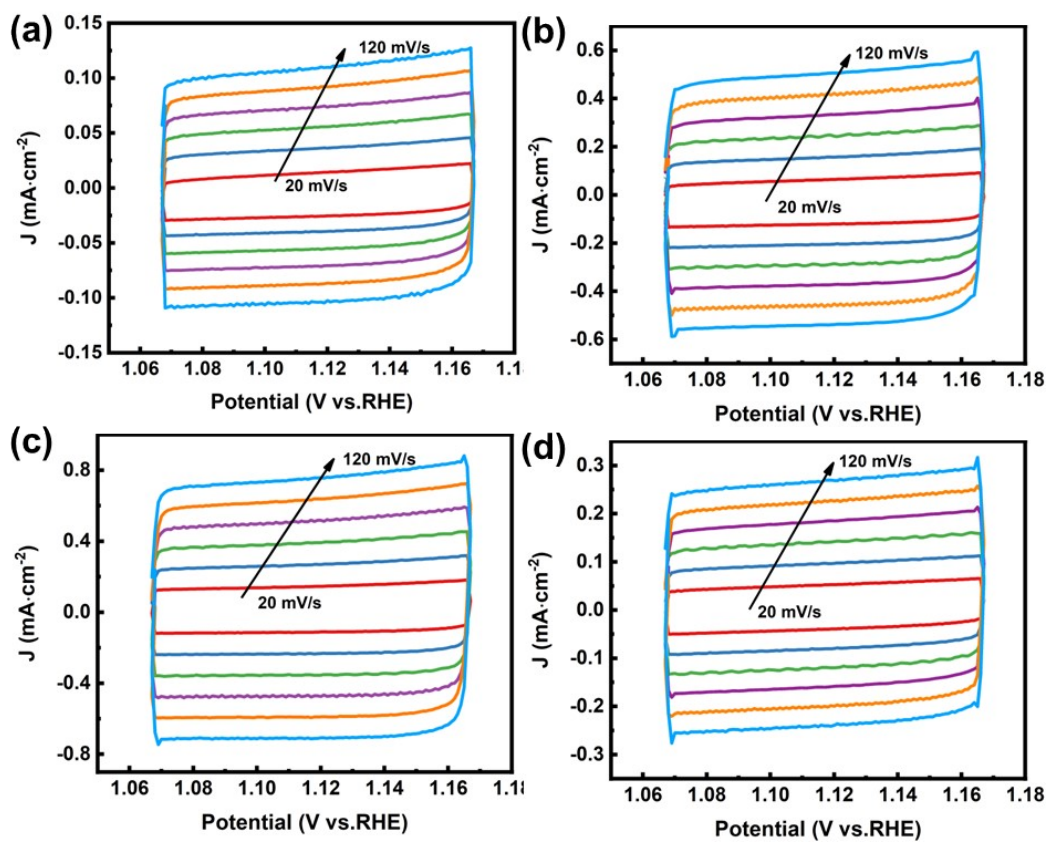
Figure S11. Cyclic voltammograms (CV) measured at scan rates of 20-120mV s^{-1} in 1 M KOH aqueous solution in the double-layer capacitor charging region: (a) a250 (b) a285 (c) a300 (d) c325.
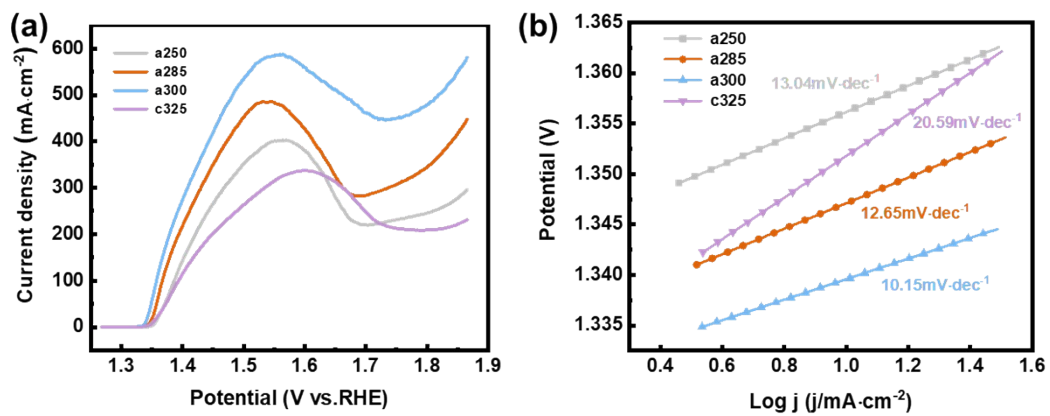
Figure S12. (a) LSV curves (b) Tafel plots of a250, a285, a300, c325 samples.
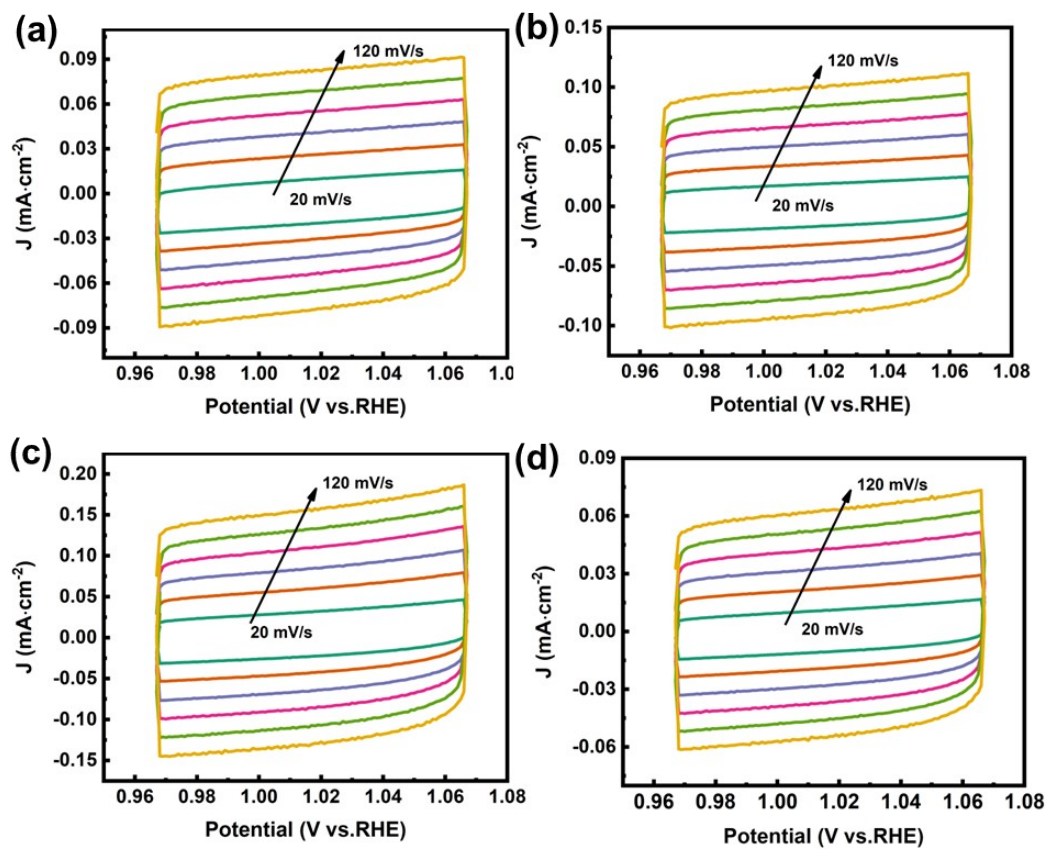
Figure S13. Cyclic voltammetric curves at different sweep rates (20-120 mV·s^{-1}) for all samples in 1 M KOH+0.33 M Urea aqueous solution: (a) a250 (b) a285 (c) a300 (d) c325.

Figure S14. The C_{dl} value calculated by ECSA fitting based on different scanning speeds of the cyclic CV curve.
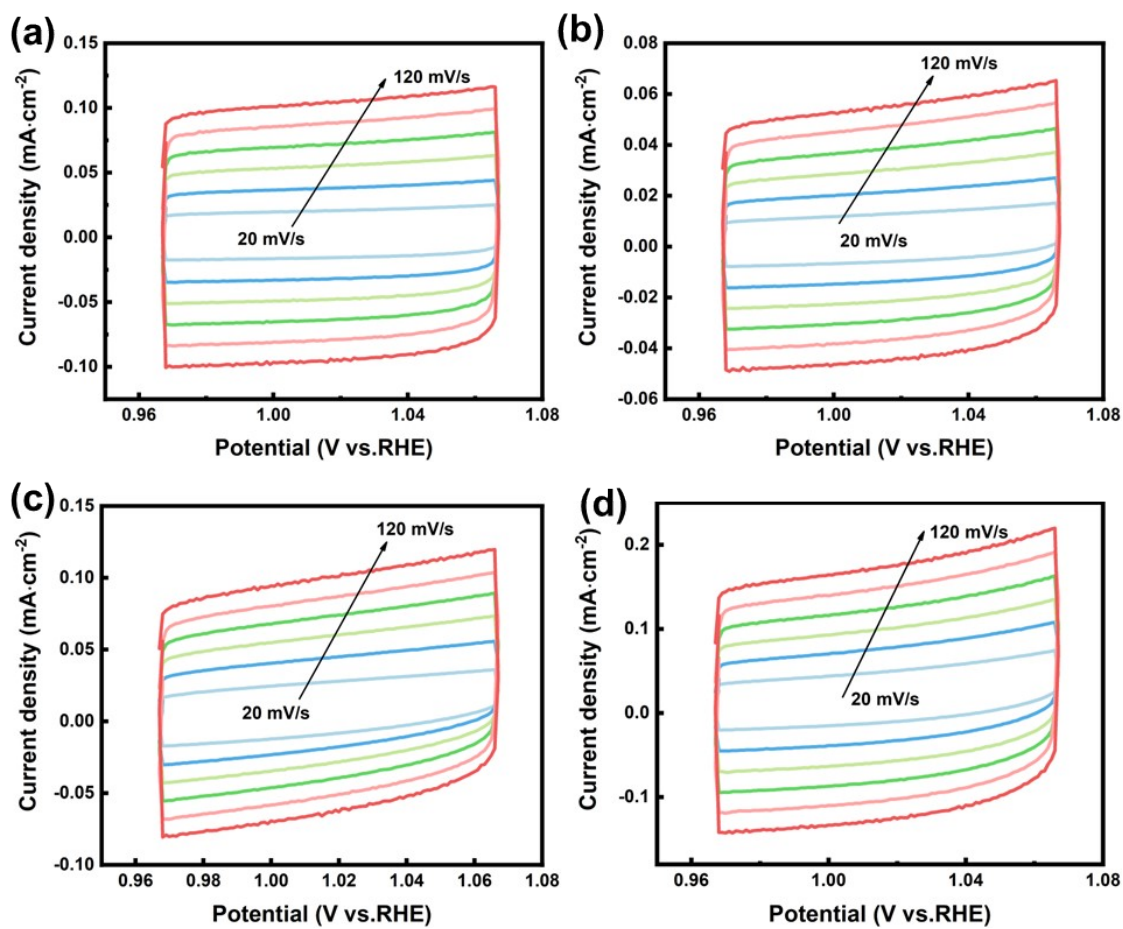
Figure S15. Cyclic voltammetric curves at different sweep rates (20-120 mV·s^{-1}) for all samples in 1 M KOH+0.5 M CH$_3$OH aqueous solution: (a) a250 (b) a285 (c) a300 (d) c325.
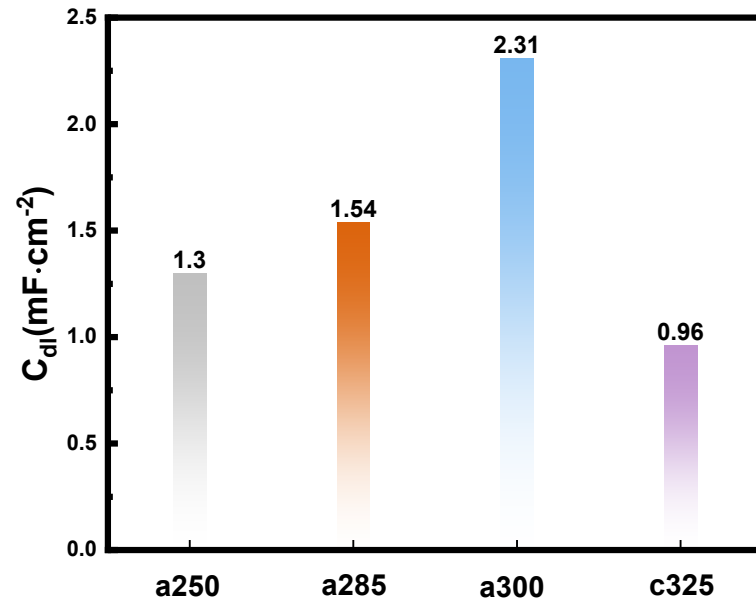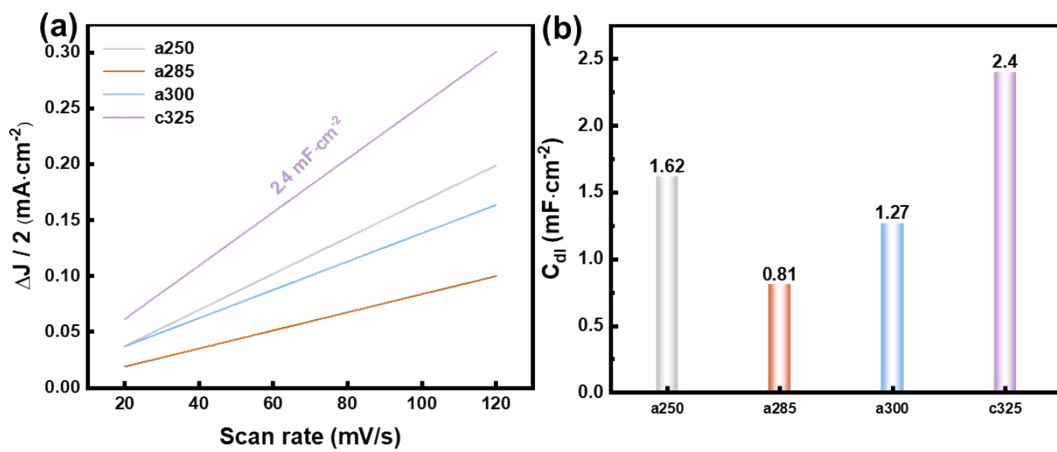
Figure S16. Electrochemical specific surface area and C_{dl} value fitting based on CV curve for all samples in 1 M KOH+0.5 M CH$_3$OH aqueous solution.
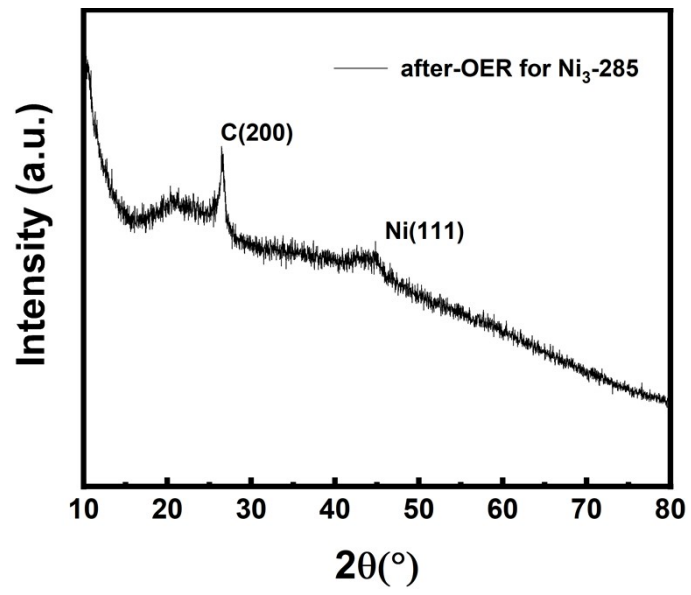
Figure S17. XRD patterns of a285 remains stable after 1000 cycles.

Figure S18. (a) Raman spectra of a250, a285, a300, c325. In situ Raman spectra of the (b)a285 (c)a300 (d) c325 catalyst collected in 1 M KOH electrolyte.

Table S3. Ni element analysis and testing of pyrolysis products (a250, a285, a300, c325).

samples	Wt(%)
a250	24.45
a285	27.79
a300	27.55
c325	30.78

Table S4. Comparison of performance of nickel based derived materials as electrocatalysts.

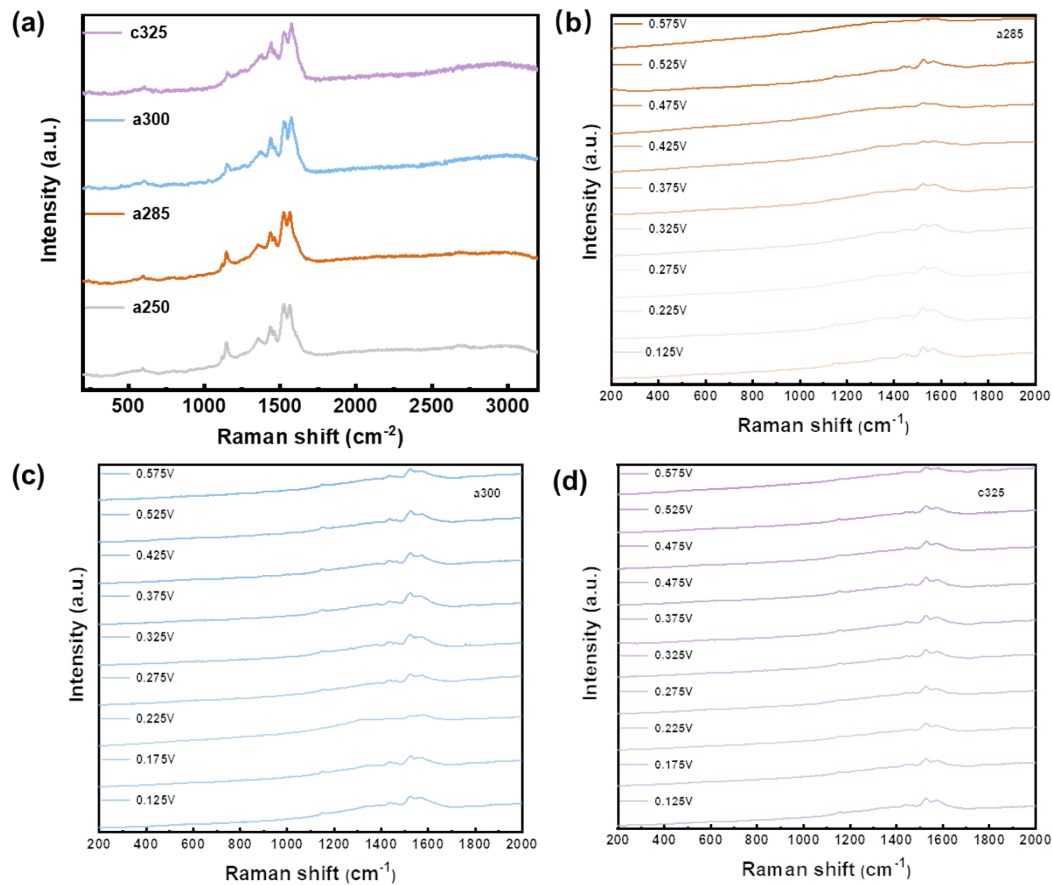| Catalysts	Current density	Reaction condition	Refs.
Ni/CeO$_2$ @CN-600	1.361 V@10 mA cm^{-2}, 1.642 V@ 229.56 mA cm^{-2}	1 M KOH + 1 M CH$_3$OH	[2]
3DNi/NiO/RG-400	specific activity (79.5 mA cm^{-2})/mass activity (1262.1 mA mg^{-1})	1 M KOH + 1 M CH$_3$OH	[3]
Pt/CeO$_2$@Ni-2	9.52 mA cm^{-2}, while that of the Pt/C catalyst only 0.59 mA cm^{-2}	0.5 M H$_2$SO4 + 1MCH$_3$OH	[4]
20% Ni-N-C	634 mA mg^{-1} at 1.55 V	1 M KOH + 1 M CH$_3$OH	[5]
Pd$_3$Ni$_1$-TaN/C	3636.36 A g$_{Pd}^{-1}$ at 1.55 V	1 M CH$_3$OH + 1 M KOH	[6]
Pt$_{99}$Ni$_1$/TiN NTs@NC	54.41 m^2 g$_{Pt}^{-1}$	0.5 M H$_2$SO$_4$ + 1 M CH$_3$OH	[7]
NiCo/N-TiO$_2$ @NaOH	73 mA cm^{-2} at 1.5 V	1 M KOH + 1 M CH$_3$OH	[8]
Pt$_3$Bi$_3$Zn NPLs	3.29 A mg^{-1}Pt	0.1 M HClO$_4$ + 0.5 M CH$_3$OH	[9]
c325	1358 mA cm^{-2} at 0.56 V	1 M KOH + 0.5 M CH$_3$OH	this work
hcp-CoNi-N/C	1.310 V vs. RHE at 10 mA cm^{-2}	1 M KOH + 0.33 M urea	[10]
Ni$_5$P$_4$/NiSe$_2$/Ni$_3$Se$_4$/NF	1.223 V at 700 mA cm^{-2}	1.0 M KOH +0.5 M urea	[11]
NiCoGe	1.4 V at 448.0 mA cm^{-2}	1 M KOH + 0.33 M urea	[12]
NiMoO$_4$ ·H$_2$O nanorods	1.32 V. at 640 mA cm^{-2}	1 m KOH + 0.33 M urea.	[13]
Ru-Co DAS/NiO	1.288 V at 10 mA cm	1 M KOH + 0.33 M urea	[14]
Ni@NCDs	1.38 V at 10 mA cm□2	1.0 M KOH + 0.5 M urea	[15]
CC/MnNi@NC	1.308 V at 10 mA cm^{-2}	1 M KOH + 0.33 M urea	[16]
P-NiMoO$_4$	1.363 V at 10 mA cm^{-2}	1 M KOH + 0.33 M urea	[17]

W-NT@NF-1	1.39	1 M KOH + 0.33 M urea	[18]
Mo-doped Ni/NiO (Ni/MNO)	1.37	1 M KOH + 0.33 M urea	[19]
Ni(OH)S/NF	1.34	1 M KOH + 0.33 M urea	[20]
a300	1.339 V at 10 mA cm^{-2}	1 M KOH + 0.33 M urea	this work
NiFe$_2$O$_4$@(Ni, Fe)P	261 mV at 10 mA cm^{-2}	1 M KOH	[21]
Ni$_2$P/FeP-FF	217 mV at 10 mA cm^{-2}	1.0 M KOH	[22]
M-NiA-CoN	180 mV at 10 mA cm^{-2}	1.0 M KOH	[23]
m-NiTPyP	267 mV at 10 mA cm^{-2}	1.0 M KOH	[24]
Ni(OH)$_2$/MoS$_2$ NF	328 mV at 10 mA cm^{-2}	1.0 M KOH	[25]
Fe-doped-Ni-(OH)$_2$	248 mV at 10 mA cm^{-2}	1.0 M KOH	[26]
FeNi(OH)x@NF	198 mV at 10 mA cm^{-2}	1.0 M KOH	[27]
Ni(OH)$_2$-FeH-STs-Ni$_3$Fe$_1$	220 mV at 10 mA cm^{-2}	1.0 M KOH	[28]
NiZnP NSs	290	1.0 M KOH	[29]
Ni(PO3)2-MoO3	234	1.0 M KOH	[30]
NiMnOP/CC	189	1.0 M KOH	[31]
Fe1Co3Mo3P-O	231	1.0 M KOH	[32]
CoNiOP/NF	245	1.0 M KOH	[33]
Fe-Co-P	269	1.0 M KOH	[34]
NiFe2O4@(Ni, Fe)P	261	1.0 M KOH	[35]
a285	197 mV at 10 mA cm^{-2}	1.0 M KOH	this work

3. References

[1]   M. R. Maurya, N. Chaudhary, F. Avecilla and I. Correia, Mimicking peroxidase activity by a polymer-supported oxidovanadium(IV) Schiff base complex derived from salicylaldehyde and 1,3-diamino-2-hydroxypropane, *J. Inorg. Biochem.*, 2015, **147**, 181-192.

[2]   J. Linghu, R. H. Guo, Y. J. Zhang, X. T. Zhang and T. P. Hu, Enhanced methanol oxidation activity of porous layered Ni/CeO2@CN nanocomposites in alkaline medium, *Appl. Surf. Sci.*, 2023, **631**, 9.

[3]   K. Zhang, Y. Han, J. Qiu, X. Ding, Y. Deng, Y. Wu, G. Zhang and L. Yan, Interface engineering of Ni/NiO heterostructures with abundant catalytic active sites for enhanced methanol oxidation electrocatalysis, *J. Colloid Interface Sci.*, 2023, **630**, 570-579.

[4]   G. Xu, Z. Ye, K. Zou, C. Li, D. Zhou, R. Lv, B. Huang, J. Li and W. Cai, Defect configuration of ceria for Pt anchoring toward efficient methanol oxidation, *Int. J. Hydrogen Energy*, 2023, **48**, 9344-9352.

[5]   Z. Zhou, J. Zhang, S. Mukherjee, S. Hou, R. Khare, M. Döblinger, O. Tomanec, M. Otyepka, M. Koch, P. Gao, L. Zhou, W. Li and R. A. Fischer, Porphyrinic MOF derived Single-atom electrocatalyst enables methanol oxidation, *Chem. Eng. J.*, 2022, **449**, 137888.

[6]   N. Ye, P. Zhao, X. Qi, R. Zhang, B. Yan, W. Sheng, Z. Jiang and T. Fang, Probing the activity origin of the enhanced methanol electrooxidation on Ni-induced PdNix(OH)y-TaN/C catalyst with nitrogen vacancies, *Appl. Catal., B*, 2023, **322**, 122142.

[7]   J. Tan, Q. Zhou, X. Zeng, G. Hu, X. Kong and Z. Pan, Platinum-Nickel alloy supported on Nitrogen-Doped carbon modified titanium nitride nanotubes derived from metalorganic frameworks as an efficient catalyst for methanol electrooxidation, *Appl. Surf. Sci.*, 2023, **607**, 154878.

[8]   N. Hoque, S. Lee, Y.-B. Park, S. Roy, M. E. A. Zaki and K. K. Bania, Ni(OH)2-SnO2 at the Hybrid Interface of Zeolite-Y and rGO for Electrochemical Oxidation of Methanol and Ethanol, *Energy & Fuels*, 2023, **37**, 11309-11318.

[9]   H. Tian, D. Wu, J. Li, J. Luo, C. Jia, Z. Liu, W. Huang, Q. Chen, C. M. Shim, P. Deng, Y. Shen and X. Tian, Rational design ternary platinum based electrocatalysts for effective methanol oxidation reaction, *J. Energy Chem.*, 2022, **70**, 230-235.

[10]   P. Li, Y. Huang, X. Ouyang, W. Li, F. Li and S. Tian, Unusual hcp Ni with metal and non-metal dual doping modulation to realize boosted urea oxidation, *Chem. Eng. J.*, 2023, **464**, 142570.

[11]   X. Xu, X. Wei, L. Xu, M. Huang and A. Toghan, Elucidating the promotion mechanism of the ternary cooperative heterostructure toward industrial-level urea oxidation catalysis, *J. Energy Chem.*, 2023, **85**, 116-125.

[12]   P. Wang, X. Bai, H. Jin, X. Gao, K. Davey, Y. Zheng, Y. Jiao and S. Z. Qiao, Directed Urea‐to‐Nitrite Electrooxidation via Tuning Intermediate Adsorption on Co, Ge Co‐Doped Ni Sites, *Adv. Funct. Mater.*, 2023, **33**, 2300687.

[13]   Y. Zhu, C. Liu, S. Cui, Z. Lu, J. Ye, Y. Wen, W. Shi, X. Huang, L. Xue, J. Bian, Y. Li, Y. Xu and B. Zhang, Multistep Dissolution of Lamellar Crystals Generates Superthin Amorphous Ni(OH)2 Catalyst for UOR, *Adv. Mater.*, 2023, **35**, 2301549.

[14]   X. Zheng, J. Yang, P. Li, Z. Jiang, P. Zhu, Q. Wang, J. Wu, E. Zhang, W. Sun, S. Dou, D. Wang and Y. Li, Dual‐Atom Support Boosts Nickel‐Catalyzed Urea Electrooxidation, *Angew. Chem.*, 2023, **135**, 2217449.

[15] Y. Pan, J. Zhang, Q. Zhang, X. Chen, Q. Wang, C. Li, Z. Liu and Q. Sun, Nickel encapsulated in carbon-dot-derived nanosheets for efficient hydrogen evolution via urea-assisted water electrolysis, *Mater. Chem. Front.*, 2023, **7**, 3340-3348.

[16] P. Li, W. Li, Y. Huang, Q. Huang and S. Tian, 3D Hierarchical‐Architectured Nanoarray Electrode for Boosted and Sustained Urea Electro‐Oxidation, *Small*, 2023, **19**, 2300725.

[17] Z.-H. Yin, Y. Huang, L.-W. Jiang, C. Meng, Y.-Z. Wu, H. Liu and J.-J. Wang, Revealing the In Situ Evolution of Tetrahedral NiMoO4 Micropillar Array for Energy‐Efficient Alkaline Hydrogen Production Assisted by Urea Electrolysis, *Small Struct.*, 2023, **4**, 2300028.

[18] M. Liu, W. Zou, S. Qiu, N. Su, J. Cong and L. Hou, Active Site Tailoring of Ni‐Based Coordination Polymers for High‐Efficiency Dual‐Functional HER and UOR Catalysis, *Adv. Funct. Mater.*, 2023, **34**, 2310155.

[19] V. Maheskumar, A. Min, C. J. Moon, R. A. Senthil and M. Y. Choi, Modulating the Electronic Structure of Ni/NiO Nanocomposite with High‐Valence Mo Doping for Energy‐Saving Hydrogen Production via Boosting Urea Oxidation Kinetics, *Small Struct.*, 2023, **4**, 2300212.

[20] J. M. Huo, Y. Wang, J. N. Xue, W. Y. Yuan, Q. G. Zhai, M. C. Hu, S. N. Li and Y. Chen, High‐Valence Metal Doping Induced Lattice Expansion for M‐FeNi LDH toward Enhanced Urea Oxidation Electrocatalytic Activities, *Small*, 2023, DOI: 10.1002/smll.202305877.

[21] Y.-l. Wang, T.-h. Yang, S. Yue, H.-b. Zheng, X.-p. Liu, P.-z. Gao, H. Qin and H.-n. Xiao, Effects of Alternating Magnetic Fields on the OER of Heterogeneous Core–Shell Structured NiFe2O4@(Ni, Fe)S/P, *ACS Appl. Mater. Interfaces*, 2023, **15**, 11631-11641.

[22] M. Jiang, H. Zhai, L. Chen, L. Mei, P. Tan, K. Yang and J. Pan, Unraveling the Synergistic Mechanism of Bi‐Functional Nickel‐Iron Phosphides Catalysts for Overall Water Splitting, *Adv. Funct. Mater.*, 2023, **33**, 302621.

[23] W. Zhang, M. Niu, J. Yu, S. Li, Y. Wang and K. Zhou, Mechanochemical Post‐Synthesis of Metal–Organic Framework‐Based Pre‐Electrocatalysts with Surface Fe□O□Ni/Co Bonding for Highly Efficient Oxygen Evolution, *Adv. Funct. Mater.*, 2023, **33**, 302014.

[24] Y. Zhang, S. Chen, Y. Zhang, R. Li, B. Zhao and T. Peng, Hydrogen‐Bond Regulation of the Microenvironment of Ni(II)‐Porphyrin Bifunctional Electrocatalysts for Efficient Overall Water Splitting, *Adv. Mater.*, 2023, **35**, 2210727.

[25] K. T. Le, N. N. T. Pham, Y.-S. Liao, A. Ranjan, H.-Y. Lin, P.-H. Chen, H. Nguyen, M. Y. Lu, S. G. Lee and J. M. Wu, Piezoelectricity of strain-induced overall water splitting of Ni(OH)2/MoS2 heterostructure, *J. Mater. Chem. A*, 2023, **11**, 3481-3492.

[26] C.-F. Li, H.-B. Tang, J.-W. Zhao and G.-R. Li, Constructing Fe/Ni atomic interfaces in Fe-doped Ni(OH)2 with single-phase structures for efficient oxygen evolution, *J. Mater. Chem. A*, 2023, **11**, 5841-5850.

[27] X. Li, C. Li, A. Yoshida, X. Hao, Z. Zuo, Z. Wang, A. Abudula and G. Guan, Facile fabrication of CuO microcube@Fe–Co3O4 nanosheet array as a high-performance electrocatalyst for the oxygen evolution reaction, *J. Mater. Chem. A*, 2017, **5**, 21740-21749.

[28] Y. Ding, B.-Q. Miao, Y. Zhao, F.-M. Li, Y.-C. Jiang, S.-N. Li and Y. Chen, Direct growth of holey Fe3O4-coupled Ni(OH)2 sheets on nickel foam for the oxygen evolution reaction, *Chin. J. Catal.*, 2021, **42**, 271-278.

[29] H. Xu, P. Song, C. Liu, Y. Zhang and Y. Du, Facile construction of ultrafine nickel-zinc oxyphosphide nanosheets as high-performance electrocatalysts for oxygen evolution reaction, *J. Colloid Interface Sci.*, 2018, **530**, 58-66.

[30] K. Li, J. Ma, X. Guan, H. He, M. Wang, G. Zhang, F. Zhang, X. Fan, W. Peng and Y. Li, 3D self-supported Ni(PO3)2–MoO3nanorods anchored on nickel foam for highly efficient overall water splitting, *Nanoscale*, 2018, **10**, 22173-22179.

[31] J. Balamurugan, T. T. Nguyen, V. Aravindan, N. H. Kim and J. H. Lee, Highly reversible water splitting cell building from hierarchical 3D nickel manganese oxyphosphide nanosheets, *Nano Energy*, 2020, **69**, 104432.

[32] Z. Li, G. Qiu, Y. Shen, X. Wang, W. Zhuang, J. Li, M. Song, P. Wang and L. Tian, Ultrafine trimetallic oxyphosphide nanoparticles for efficient electrochemical overall water splitting, *J. Alloys Compd.*, 2020, **820**, 153161.

[33] L. Yang and L. Zhang, Interfacial electronic modification of bimetallic oxyphosphides as Multi-functional electrocatalyst for water splitting and urea electrolysis, *J. Colloid Interface Sci.*, 2022, **607**, 546-555.

[34] H. Zhang, W. Zhou, J. Dong, X. F. Lu and X. W. Lou, Intramolecular electronic coupling in porous iron cobalt (oxy)phosphide nanoboxes enhances the electrocatalytic activity for oxygen evolution, *Energy Environ. Sci.*, 2019, **12**, 3348-3355.

[35] Y. Wang, Y. Wang, H. Gao, Z. Huang, Q. Hao and B. Liu, Interface-induced contraction of core–shell Prussian blue analogues toward hollow Ni-Co-Fe phosphide nanoboxes for efficient oxygen evolution electrocatalysis, *Chem. Eng. J.*, 2023, **451**, 138515.